Quantum Projectors Implemented With Optical Directional Couplers in Ion-Exchanged Glasses

Xesús Prieto-Blanco [ID], Carlos Montero-Orille [ID], Jesús Liñares [ID], Héctor González-Núñez [ID], and Daniel Balado

(Integrated Photonics 2022)

Abstract—**Ion-exchanged glass as a platform for quantum photonics is proposed. Quantum projectors are implemented with integrated optical directional couplers fabricated by ion-exchange K^+/Na^+ in soda-lime glass. We consider devices composed of concatenated directional couplers which implement N-dimensional quantum projective measurements, and concomitantly the production of 1-qudit states. The fundamental units of these devices are 2 $\times$ 2 directional couplers that are experimentally studied in order to obtain, through an optical characterization, empiric relationships between fabrication and optical parameters of such couplers. Likewise, a two-dimensional quantum projector is demonstrated so that projective measurements are obtained for the states of bases X (diagonal) and Y (circular).**

Index Terms—**Integrated quantum passive elements, integrated quantum projective meters, ion-exchanged glass platform.**

I. INTRODUCTION

INTEGRATED quantum photonic devices can implement different quantum operations for quantum communications, quantum computation, quantum metrology, and so on, with the inherent advantages associated to integrated optics. Different platforms have been proposed and used to develop these integrated quantum devices, including silicon-on-insulator (as SiO_2), Lithium Niobate, and Gallium Arsenide [1]–[3]. However, to our knowledge, ion-exchanged glass (IExG) platform has not been used as an integration technology for quantum photonics, despite the fact that it is present in many classical optical communications systems and optical sensors, and has been

Xesús Prieto-Blanco and Jesús Liñares are with the Quantum Materials and Photonics Research Group, Optics Area, Applied Physics Department, Faculty of Physics/Faculty of Optics and Optometry, Universidade de Santiago de Compostela, E-15782 Santiago de Compostela, Galicia, Spain, and also with the iMA-TUS, Institute of Materials, Universidade de Santiago de Compostela, E-15782 Santiago de Compostela, Galicia, Spain (e-mail: xesus.prieto.blanco@usc.es; suso.linares.beiras@usc.es).

Carlos Montero-Orille, Héctor González-Núñez, and Daniel Balado are with the Quantum Materials and Photonics Research Group, Optics Area, Applied Physics Department, Faculty of Physics/Faculty of Optics and Optometry, Universidade de Santiago de Compostela, E-15782 Santiago de Compostela, Galicia, Spain (e-mail: carlos.montero@usc.es; hector.gonzalez.nunez@usc.es; daniel.balado.souto@usc.es).

suggested several years ago for this task [4]. It is well known that this platform has advantages with respect to cost, technological requirements, and fibre optical compatibility [5]. Moreover, it can also be reconfigurable in a thermo-optical way [6]. In this work we show the implementation of passive quantum optical projectors with integrated optical elements in IExG platform. We must stress that passive integrated optical elements for certain applications present clear advantages respect to, for instance, electro-optical elements, such as energy saving and no complex geometries of electrodes required.

Projective measurements are the most common way to detect quantum states, in general, and quantum light states, in particular. It is an important task in most of quantum optical circuits intended for quantum computation, quantum cryptography, and quantum processing [7], [8]. Likewise, generalized measurements as POVMs (Positive operator-valued measurements) are required to obtain an unambiguous quantum non-orthogonal state discrimination. Projective measurements are a particular case of POVMs [9]. In the case of quantum communications, quantum light states propagate in optical fibres, or free space, and can be excited in codirectional optical modes, such as those of Multi-Core optical Fibres (MCF) [10]–[12], or in collinear optical modes, such as those of Few Mode optical Fibres (FMF) [13], [14]. Moreover, codirectional modes coming from MCFs can be easily coupled to an integrated optical circuit. Therefore, such circuits are ideal candidates to perform quantum transformations and, in particular, the quantum projective measurements mentioned above. We call this type of circuits as integrated quantum optical circuits (IQOCs). In addition, this solution can be extended to collinear modes. For that, a prior spatial demultiplexing process, along with the use of modal converters, is required in order to get a spatial separation of optical modes, which facilitates their coupling to an IQOC. Photonic lanterns can implement such operations in a compact form [15]. Accordingly, the implementation of the mentioned quantum transformations and/or projective (or POVMs) measurements can be made. As commented, these quantum circuits can perform different transformations, but projective measurements are usually required in the final part of quantum communications systems (Bob system). In this work we focus on these projective —and also generalized— measurements used for quantum cryptography in optical fibres [7], [11], [12], although other applications are also possible, in quantum computation (for specific purposes) [1], [3], [16], quantum simulations [8], [17], [18], QRW [16],

[19], [20], quantum metrology and sensors [21]–[23], and so on.

IQOCs, for N-dimensional quantum spaces, can be realized with integrated optical elements as single mode channel waveguides (SMW), directional couplers and integrated phase shifters [24]–[27]. So, integrated quantum optical projectors (IQOPs) can be implemented with these integrated optical elements and, therefore, an experimental realization of these projectors is an important and relevant task. Here, we propose the experimental use of IExG platform for implementing IQOPs, although many other quantum components could be implemented, such as quantum simulators [28], quantum random walk, and so on. These implementations will be efficient as long as a few qubits are considered, which is related to the well-known scalability difficulty of quantum integrated photonics. In particular, we propose passive quantum projectors implemented with concatenated optical directional couplers and phase shifters fabricated by K^+/Na^+ ion-exchange processes in soda-lime glass. Since these projectors are intended for quantum cryptography purposes, they are designed in such a way that a quantum random choice of measurement basis is done [12]. The fundamental or basic unit of these projectors is the 2x2 directional coupler, that is, $N = 2$. Therefore, we present the results of fabrication as well as the optical tests of such couplers. In particular, we make a semiclassical test of projective measurements of the quantum states belonging to bases X and Y. The results show that IExG is a platform with enough advantages to be used in quantum technology along with other platforms.

The organization of the paper is as follows. In Section II we present the theoretical fundamentals on passive quantum projectors with random choice of measurement basis, as required in most of the quantum cryptography protocols. In particular, we introduce this kind of projectors with the case $N = 2$, although their generalization to an arbitrary dimension is quite straightforward. Next, in Section III, the fabrication of a 2x2 projector by IExG is described, specifically, by a K^+/Na^+ ion-exchange process in soda-lime glass, and paying special attention to the experimental curves obtained in order to determine the fabrication parameters of the circuit. In Section IV, an optical test of a basic projector 2x2 is shown. This includes the use of an external optical grating to change the basis of quantum states and shows, in a semiclassical way, that projective measurements can be realized. Finally, in Section V, conclusions are presented.

II. PASSIVE QUANTUM PROJECTORS BASED ON DIRECTIONAL COUPLERS

The quantum light states with a major interest are the single photon states —which are, for instance, used in quantum cryptography— and, in particular, 1-qubit (two optical modes) and 1-ququart states (four optical modes). In fact, 1-ququart states are the states which give rise to the beginning of the so-called high-dimensional quantum cryptography with 1-qudit, that is, quantum states of dimension d, which can be implemented with a number N of optical modes (or optical paths), that is, $d = N \geq 2$:

$$|L\rangle = \sum_{j=1}^{d=N} c_j |000\ldots1_j\ldots000\rangle = \sum_{j=1}^{d=N} c_j |1_j\rangle, \qquad (1)$$

where, in addition, the states have to belong to the so called mutually unbiased bases (MUBs), that is, $|c_1| = \ldots = |c_j| = \ldots = |c_N| = 1/\sqrt{N}$. A source of single photons can be obtained from SPDC (spontaneous parametric down-conversion) sources [8] or even from lasers, that is, from multimode coherent states $|\alpha_1\ldots\alpha_N\rangle$ with a very low photonic excitation (weak coherent states), that is, $|\alpha_j| \ll 1$, therefore,

$$|L\rangle \approx |0\rangle + \sum_{j=1}^{N} \alpha_j |000\ldots1_j\ldots000\rangle. \qquad (2)$$

Let us start by considering the case of a two-dimensional quantum problem, that is, $N=2$, so 1-qubit states will be used. This case will help us to explain the implementation of integrated quantum optical projectors. As commented, the fundamental units of these devices are the synchronous directional couplers along with integrated phase shifters. It is well known that synchronous directional couplers can be represented by the following matrix:

$$X_\theta = \begin{pmatrix} \cos\theta & i\sin\theta \\ i\sin\theta & \cos\theta \end{pmatrix}, \qquad (3)$$

where the coupling phase is $\theta = \kappa l$, with κ the coupling coefficient and l the length of the coupler. For a two-dimensional IQOP the required couplers are, by one hand, a $X_{\pi/4}$, that is, a 3 dB (or 1:1) coupler, which corresponds to the logic gate $\sqrt{X}$ and, on the other hand, a $X_{\pi/2}$ corresponding to the usual logic gate X. Moreover, phase shifters are required, that is,

$$Z_\Phi = \begin{pmatrix} 1 & 0 \\ 0 & e^{i\Phi} \end{pmatrix}. \qquad (4)$$

Phase shifters $Z_{\pi/2}$ and Z_π are usually needed. So, by concatenating X_θ and Z_Φ elements, we can implement complex and fully operational IQOPs. For example, let us consider the bases X and Y with the following single photon states excited in two channel waveguides j and j',

$$X = \{|1_D\rangle, |1_A\rangle\} = \left\{ \frac{1}{\sqrt{2}}(|1_j\rangle + |1_{j'}\rangle), \frac{1}{\sqrt{2}}(|1_j\rangle - |1_{j'}\rangle) \right\}, \qquad (5)$$

$$Y = \{|1_L\rangle, |1_R\rangle\} = \left\{ \frac{1}{\sqrt{2}}(|1_j\rangle + i|1_{j'}\rangle), \frac{1}{\sqrt{2}}(|1_j\rangle - i|1_{j'}\rangle) \right\}. \qquad (6)$$

If these channel waveguides are coupled by a coupler $X_{\pi/4}$ then a IQOP is implemented for the basis Y, that is, the input states $|1_L\rangle$ and $|1_R\rangle$ become the states $|1_{j'}\rangle$ and $|1_j\rangle$, respectively, at the output. Likewise, the IQOC defined by $X_{\pi/4}Z_{\pi/2}$ implements an IQOP for the basis X, that is, the input states $|1_D\rangle$ and $|1_A\rangle$ also become the states $|1_{j'}\rangle$ and $|1_j\rangle$, respectively, at the output.

On the other hand, a random choice of the measurement basis is required in quantum cryptography. For that, a more complex integrated circuit is needed. In Fig. 1 we draw an IQOC with four paths, $j = 1$–4, for making projective measurements of states in the basis X or Y in a random way. Indeed, let us consider 1-qubit input states, in a vector representation (c_1, c_3), coming from a transmission line where a Quantum Key Distribution (QKD) is distributed, as for example by the BB84 protocol (see,
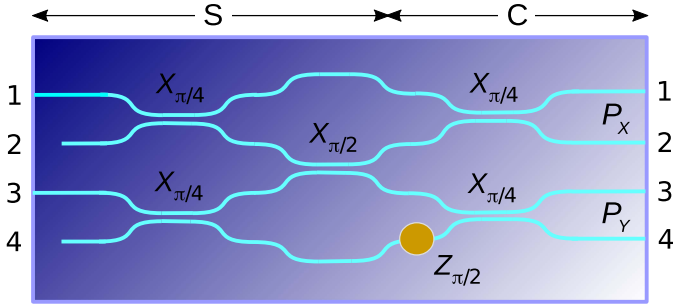
Fig. 1. Drawing of an integrated quantum optical projector for the two-dimensional bases X and Y.

for instance, [29]). Likewise, let us consider that these 1-qubit states are excited in paths (optical modes) 1 and 3, that is,

$$|L\rangle = c_1|1_1\rangle + c_3|1_3\rangle. \tag{7}$$

The first part of the IQOC (S in Fig. 1) is formed by two couplers $X_{\pi/4}$ and one coupler $X_{\pi/2}$. They implement the following operation:

$$\mathbb{S}|L\rangle = \frac{1}{\sqrt{2}}\begin{pmatrix} 1 & i & 0 & 0 \\ 0 & 0 & i & -1 \\ -1 & i & 0 & 0 \\ 0 & 0 & i & 1 \end{pmatrix}\begin{pmatrix} c_1 \\ 0 \\ c_3 \\ 0 \end{pmatrix} = \frac{1}{\sqrt{2}}\begin{pmatrix} c_1 \\ ic_3 \\ -c_1 \\ ic_3 \end{pmatrix} \tag{8}$$

which is a state division that ensures a random choice of the measurement basis. Note that this operation generates a relative phase $\pi/2$ between paths 1 and 2, and $-\pi/2$ between paths 3 and 4. These phases must be taken into account in the projective measurement. In particular, the former is equivalent to a gate $Z_{\pi/2}$ between paths 1 and 2. So, a projective operation in the basis X is performed after the top right $X_{\pi/4}$ coupler of Fig. 1: $P_X = X_{\pi/4}Z_{\pi/2}$. Similarly, a projection in the basis Y is obtained in the subspace formed by path modes 3 and 4, by cancelling their relative phase -$\pi/2$ by a gate $Z_{\pi/2}$ in path 4, before the bottom right $X_{\pi/4}$ coupler: $P_Y = X_{\pi/4}$. The matrix associated with this second part of the IQOC (C in Fig. 1) is given by

$$\mathbb{C} = \frac{1}{\sqrt{2}}\begin{pmatrix} 1 & i & 0 & 0 \\ i & 1 & 0 & 0 \\ 0 & 0 & 1 & -1 \\ 0 & 0 & i & i \end{pmatrix}. \tag{9}$$

Therefore, the whole circuit implements the following projective transformation:

$$\mathbb{P} = \mathbb{C}\mathbb{S} = \frac{1}{2}\begin{pmatrix} 1 & i & -1 & -i \\ i & -1 & i & -1 \\ -1 & i & -i & -1 \\ -i & -1 & -1 & i \end{pmatrix}. \tag{10}$$

As an example, let us consider the input state $|L\rangle = |1_D\rangle = (1/\sqrt{2})(|1_1\rangle + |1_3\rangle)$, then the state division operation implemented by $\mathbb{S}$ gives the state $\mathbb{S}|1_D\rangle = (1/\sqrt{2})(|1_1\rangle + i|1_2\rangle - |1_3\rangle + i|1_4\rangle)$ and, next, the action of $\mathbb{C}$ gives the output state

Fig. 2. Drawing of an integrated quantum optical circuit for implementing a POVM for states $|L_\pm\rangle = \cos\alpha|1_1\rangle \pm i\sin\alpha|1_2\rangle$.

$\mathbb{P}|1_D\rangle = (i/\sqrt{2})|1_2\rangle - (1/2)e^{i\pi/4}(|1_3\rangle + |1_4\rangle)$. That is, the state $|1_D\rangle$ is projected on exit 2. Note that a detection on exits 3 and 4 will be discarded by Bob's system after Alice communicates the measurement basis (X, in this case) [29]. Likewise, the state $|1_A\rangle$ becomes $\mathbb{P}|1_A\rangle = (1/\sqrt{2})|1_1\rangle - (1/2)e^{-i\pi/4}(|1_3\rangle - |1_4\rangle)$, and is projected on exit 1. Therefore the states of basis X are measured at output channel guides 2 and 1. Similarly, the states $|1_L\rangle$ and $|1_R\rangle$ of the Y-basis are measured at output channel guides 4 and 3, respectively. In short, we formally have a projective operation P_X for states of the basis X in the subspace defined by modes 1 and 2, and another one P_Y for the states of basis Y in the subspace defined by modes 3 and 4 (see Fig. 1). Therefore this IQOC works as a passive IQOP with random choice of measurement basis, where the $X_{\pi/4}$ and $X_{\pi/2}$ couplers can be regarded as its basic functional units. Their fabrication in an IExG platform will be shown in the next section.

On the other hand, it is worth showing that generalized measurements can be also implemented with these circuits based on directional couplers. The projective measurement described above are useful for orthogonal states. However, in some cases, non orthogonal states are produced and, therefore, a different measurement approach has to be used. Positive operator-valued measurement (POVM) is one of the generalized measurement approach for non orthogonal states. Let us consider, for example, the following non-orthogonal states in the subspace of two path modes (two integrated channel guides):

$$|L_\pm\rangle = \cos\alpha|1_1\rangle \pm i\sin\alpha|1_2\rangle. \tag{11}$$

Note that $|\langle L_+|L_-\rangle| = \cos 2\alpha \neq 0$. If $\alpha = \pi/4$ then we obtain the orthogonal states $|1_{\left(\frac{L}{R}\right)}\rangle$. By following the POVM proposed in [30] for polarization modes, we can implement a POVM for quantum states given by (11), which are excited in path modes. A sketch of a circuit to implement this kind of measurement is shown in Fig. 2. The circuit is made of a directional coupler X_θ, in the space of path modes 0-1, followed by a directional coupler $X_{\pi/4}$. Again, the calculation of the total action of the circuit gives the following matrix:

$$\mathbb{M} = \begin{pmatrix} \cos\theta & i\sin\theta & 0 \\ i\sin\theta & \cos\theta/\sqrt{2} & i/\sqrt{2} \\ -\sin\theta/\sqrt{2} & i\cos\theta/\sqrt{2} & 1/\sqrt{2} \end{pmatrix}. \tag{12}$$

Next, the action on the states $|L_\pm\rangle$ has to discriminate between them, that is, $\cos\theta = \tan\alpha$. Then, the directional coupler X_θ must meet $\theta = \cos^{-1}(\tan\alpha) = \kappa L$, which can be achieved experimentally as we will see in Section IV. Therefore, the

following transformation is obtained

$$\mathbb{M} = \frac{1}{\sqrt{2}\cos\alpha}\begin{pmatrix} \sqrt{2}\sin\alpha & i\sqrt{2\cos 2\alpha} & 0 \\ i\sqrt{2\cos 2\alpha} & \sin\alpha & i\cos\alpha \\ -\sqrt{2\cos 2\alpha} & i\sin\alpha & \cos\alpha \end{pmatrix}. \quad (13)$$

Note that the vectors defined by (M_{22}, M_{23}) and (M_{32}, M_{33}) are the vector representation of the bras $\langle L_\pm^\perp|$. Therefore, in the subspace of path modes 1-2, the following POVM operators are implemented

$$\hat{\pi}_\pm = \frac{|L_\pm^\perp\rangle\langle L_\pm^\perp|}{1 + |\langle L_+|L_-\rangle|} \quad (14)$$

and the measurement is obtained in detectors D_+ and D_-. Indeed, for the state $|L_+\rangle$ the output state is $\mathbb{M}|L_+\rangle = i\sqrt{2\cos 2\alpha}|1_0\rangle + i(\sin 2\alpha/\sqrt{2}\cos\alpha)|1_2\rangle$. So, if detector D_- clicks then the state $|L_+\rangle$ is measured, with a probability $2\sin^2\alpha$, such as the general theory predicts. That is, $\langle L_+|\hat{\pi}_+|L_+\rangle = 0$ and $\langle L_-|\hat{\pi}_+|L_-\rangle = 2\sin^2\alpha$. The detector D_0 corresponds to the case of non conclusive outcome, that is, the outcome governed by the operator $\hat{\pi}_0 = \mathbb{I} - \hat{\pi}_+ - \hat{\pi}_-$. In short, an additional path mode, corresponding to the channel guide 0 shown in Fig. 2, together with the coupler X_θ with $\cos\theta = \tan\alpha$, implements a POVM for states $|L_\pm\rangle$. A similar POVM can be implemented for the states $|L_\pm'\rangle = \cos\alpha|1_1\rangle \pm \sin\alpha|1_2\rangle$.

III. FABRICATION OF A 2x2 PROJECTOR BY ION-EXCHANGE IN GLASS

This section focuses on the fabrication of the $X_{\pi/4}$ and $X_{\pi/2}$ basic units composed of 2x2 directional couplers. These units were fabricated by thermal ion-exchange K$^+$/Na$^+$ in glass together with photolithographic procedures to generate the suitable patterns. As it is well known, ion exchange modifies the chemical composition of appropriate substrates and, as a consequence, waveguides can be created using this technique. The ion-exchange procedure that we have used is similar to that presented in [31], where the authors carried out a selective ion-exchange followed by a planar one. However, we used a burial process as the second step. This choice presents some advantages which we will comment below. With respect to the photolithographic procedure, we produced a metal mask with several basic units, each having a different geometry. So, modal coupling empiric curves —and the required directional coupler— could be obtained, once a particular set of parameters of the ion-exchange process was selected. Note that, usually, photolithographic parameters are selected and the ion-exchange parameters are changed. Next, we explain the details of the fabrication process.

At first, let us consider a non-masked glass substrate containing sodium ions. If this substrate is dipped into a salt (KNO$_3$, for example) at a high temperature T, the Na$^+$ ions of the glass are exchanged for the K$^+$ ions of the salt. As a result, the refractive index of the glass increases in a micrometric layer beneath the glass surface and an integrated waveguide can be obtained. In addition, some birefringence arises from the mechanical stresses due to the difference in size of K$^+$ and Na$^+$ cations [32]. A subsequent thermal diffusion can be used to carry out a burial
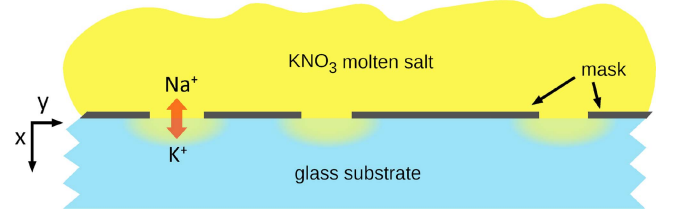

Fig. 3. Sketch of a selective ion-exchange process.

process of this waveguide by immersing the substrate into a molten salt containing sodium ions (NaNO$_3$, for example). So, the Na$^+$ ions present in the salt replace the most surface doping cations K$^+$ and the refractive index at the glass surface drops to its original value. This second step, i.e. the burial process, is not mandatory but presents two great advantages. First, the modal field is located further from the glass surface, which can present irregularities, and so losses are reduced [33]. Second, it reduces the typical anisotropy of K$^+$/Na$^+$ ion-exchange waveguides since the accumulated mechanical stresses are diminished [34]. On the other hand, if a selective ion-exchange is required to produce, for example, channel waveguides, a suitable mask can be patterned on the glass surface by some lithographic method (see Fig. 3). This is the case of directional couplers, which are usually formed by single-mode channel waveguides. The dimensions of these waveguides are determined by the penetration of ions, both in the x-direction (in-depth diffusion) and in the y-direction (side diffusion), as well as the size of the openings of the metal mask. Fig. 3 shows a sketch of a selective ion-exchange process where the mask, the molten salt, and both the in-depth and side diffusion of ions are drawn. Note that the burial step is carried out after mask removal.

In order to select appropriate fabrication parameters (mainly the ion-exchange time, t), we adopted the effective index method (EIM) [24], [35], [36] together with a separability approximation, justified by the weak guidance. Thus, we obtained the single-mode condition in the y-direction, while in the x-direction, it was studied experimentally through the optical characterization of slab waveguides. With regard to the fabrication of the metal mask, a two-step photolithographic process was used [37]. In the first step, different coupler patterns were plotted on a sheet of heavy paper and then reduced -1/14.11 by using a lens Schneider XENON Sapphire 4.5/95. This lead to an aluminium master on a glass substrate that was then reduced by a Carl Zeiss S-planar lens working at magnification M=-1/5 and $f/\#$=1.3. Despite this two-step process, we were not able to get minimum mask widths less than 3 μm, which prevented us from making channels narrower than this amount. Moreover, the side diffusion also widens the lateral size of the channel waveguide (see Fig. 3). Therefore, we made an estimate of this side diffusion and assumed that it is equal to the penetration depth. We used soda-lime glasses with refractive index n_s=1.5104 for the working wavelength λ_o=632.8 nm. From previous studies [31], we set the temperature of both the first ion-exchange and the burial process to T=400 °C. Several thermal ion-exchanges in test glasses without metal masks were made and the effective
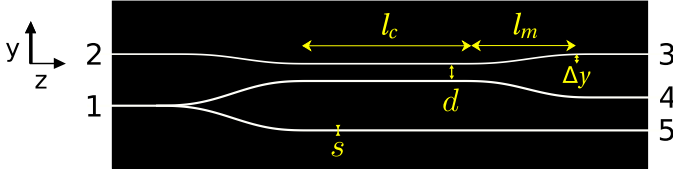
Fig. 4.   Basic integrated optical element (BIOE) for optical characterization purposes.

indices of the modes of the waveguides were measured by prism coupling (also known as M-lines method). This was done with an automated system (Metricon, Model 2010/M). From these measurements, and taking into account the numerical results provided by the EIM, we set a time of t_1=30 min for the first ion-exchange and t_2=10 min for the burial process. These parameters lead to waveguides with a single mode of effective index N_{eff}=1.5117.

As stated before, the design and fabrication of IQOPs need a prior optical characterization of the full fabrication process of the basic units $X_{\pi/4}$ and $X_{\pi/2}$. For that we used a basic integrated optical element (BIOE) which is shown in Fig. 4. It consists of a set of three waveguides of width s forming a Y-junction and a directional coupler which will be object of optical characterization. The Y-junction begins in the waveguide 1 and has the purpose of providing a reference signal [38] in waveguide 5 after a 50%-50% split. Next, the waveguide 2 and one of the waveguides of the Y-junction are approached through a Minford curve [39],

$$y = \Delta y \left[\frac{z}{l_m} - \frac{1}{2\pi} \sin\left(2\pi \frac{z}{l_m} \right) \right], \qquad (15)$$

with Δy=15.4 μm and l_m=1520 μm, defining a directional coupler. Once the ion-exchange fabrication parameters are fixed (temperature, time, salt, ionic concentration, and glass substrate), the spatial parameters d (distance between coupled channel waveguides) and l_c (coupling length), shown in Fig. 4, will determine the optical characteristics of the couplers. In order to determine d and l_c for a particular coupler, a calibration method is used, that is, the design of the mask includes a series of BIOEs with different d and l_c. This has a double objective. By one hand, it ensures that some of the BIOEs can become equal or quite close to the remarkable couplers $X_{\pi/4}$ or $X_{\pi/2}$. On the other hand, it makes possible to obtain the empiric curves of these parameters that in turn will allow us to design couplers with the desired coupling percentage in a subsequent fabrication process. So, we have designed a mask containing 16 BIOEs in 4 blocks. In each block, d is fixed while l_c varies. These values, after the photo-reduction process, are found in the interval $d \in [3, 7.5]$ μm and $l_c \in [0.5, 2]$ mm. The results of the optical characterization of the BIOEs and the empiric curves of the fabrication parameters are analysed and shown in the next section. We must indicate that the side diffusion increases the width of the channel guides up to 4 μm with respect to the 3 μm of the mask openings. Furthermore, these BIOEs were designed to introduce light through end-fire coupling. Consequently, the waveguides have been ended in flat and polished faces, perpendicular to their propagation axis.

IV. SEMICLASSICAL DEMONSTRATION AND TEST OF A 2x2 PROJECTOR

A. Optical Characterization System

The optical characterization of the BIOEs begins with a visual inspection, through a microscope, of the aluminium mask. Usually, some of the BIOEs have breaks or irregularities in the mask openings of a few micrometers in length. One would expect that they would have to be discarded. However, all of them worked well, showing that this technology has excellent tolerance to mask defects. Next, the end-fire coupling technique is used to couple light to the input channel waveguides and, after propagation through the BIOE, to observe it at the outputs. A sketch of the optical setup used for this task is shown in Fig. 5. It is similar to the system described in reference [40] but, in this one, it is especially important the subsystem that includes, together with the microscope objectives, a light-emitting-diode (LED), two beam splitters (BS), and an eyepiece. It allows us to watch simultaneously the back-reflected beams on the input face of the BIOE as well as the channel waveguides illuminated by the LED. This makes the coupling process easier through a three-axis translation stage and, for fine positioning, a low-power positive lens L1 that can be moved up and down.

If the Gaussian beam on the input face of the BIOE has the appropriate height and waist, it will match the fundamental mode of the channel waveguide and a high coupling to this mode will be obtained. In our case, the required waist of the beam was wider than the 10× objective resolution; then we arranged the system so that the beam illuminated only the central region of the objective aperture stop. On the other side of the BIOE, a 20× microscope objective images the exit face on a CMOS Thorlabs DCC1545 M camera. We have chosen a camera as the measuring instrument, instead of a power meter, because the extension of the output beams is comparable to their separation. With a power meter, it would be difficult to individualize the power measurements of each output beam. Likewise, the temporal evolution of the measurements can be studied easily with a camera and their values are not affected by the temporal fluctuations of the laser. Moreover, this CMOS camera exhibits a good linear response up to saturation, which ensures a true relative power measurement [41]. On the other hand, two polarisers were inserted in this setup to work with a specific polarization (TE or TM). First polariser ensures the polarization state at the entrance of the waveguides. The second one, placed in front of the CMOS camera, allows us to distinguish between polarization states at the output, since K^+/Na^+ ion-exchanged waveguides in glass, after burial processes, can still have a certain anisotropy.

B. Optical Characterization Results

The characterization of the modal coupling in the BIOEs (16 units) was made by using the optical system described in the previous subsection. The light from the He-Ne laser is coupled to input waveguide 1 of each BIOE, that is, a coherent state $|\alpha\rangle$ is used. Then, as mentioned above, the Y-junction splits the light into two halves: one of them goes through the reference waveguide 5 and the other one through waveguide 4 which is a part of the coupler. So, three modal outputs 3, 4, and 5 are
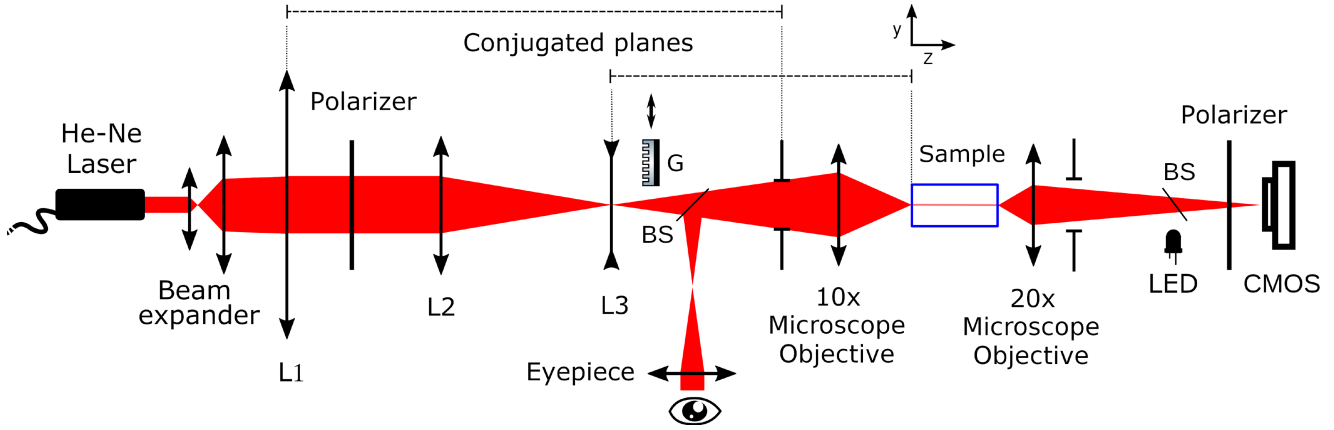
Fig. 5. Sketch of the optical setup used for the characterization of the BIOEs.
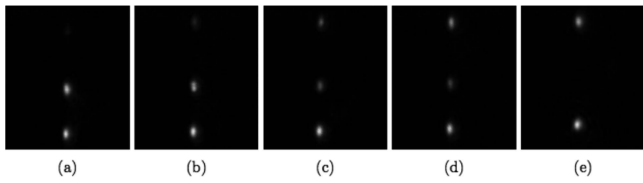

Fig. 6. Images obtained by a CMOS camera of the output of different BIOEs after coupling TE polarized light into input 1 (Y-junction). The lower point corresponds to the output of the reference waveguide (5), while the two upper points are the outputs of the coupler waveguides (3 and 4). (a) Light exits by output 4 ($\theta = 2n\pi$). (e) Light exists by output 3 ($\theta = (2n+1)\pi/2$). (c) Light exits by both outputs 3 and 4 ($\theta = (2n+1)\pi/4$). (b) and (d) are intermediate cases.

TABLE I
COUPLING RESULTS EXPRESSED AS POWER RATIOS
($P_4/(P_3+P_4)|P_3/(P_3+P_4)$) IN PERCENTAGES AT OUTPUTS 4 AND 3

BIOEs Series		l_c (mm)		
		0.5	1.0	1.5	2.0
	3.0	(17.8|82.2)	(93.6|6.4)	(54.9|45.1)	(2.5|97.5)
$d(\mu m)$	4.5	(35.9|64.1)	(5.9 |94.1)	(7.4|92.6)	(40.9|59.1)
	6.0	(80.7|19.3)	(63.8|36.2)	(49.3|50.7)	(26.8|73.2)
	7.5	(92.6| 7.4)	(88.4|11.6)	(86.3|13.7)	(79.8|20.2)

observed on the CMOS camera. Next, by taking several pictures and processing them with a suitable software, the amount of light which comes out of each of the three waveguides can be evaluated. In particular, the relative percentage of power that leaves the waveguides (3 and 4) of the coupler can be calculated and compared to itself when light is coupled into input 2. We did this comparison for the sixteen different BIOEs of the sample and for TE polarization. Qualitatively, we saw that the results are similar for TM polarization. The presence of anisotropy in the waveguides made the measurements a bit difficult, detecting in some cases some energy transfer from TE to TM modes. Anyway, the energy transferred was small and its inclusion in the analysis did not change substantially the coupling results. In Fig. 6 some examples of images taken during the optical characterization process of the BIOEs are presented.

Measurements of the powers that come out of outputs 4 and 3 are shown in Table I as percentages of power ratios, that is, $P_4/(P_3+P_4)$ and $P_3/(P_3+P_4)$. These values, according to
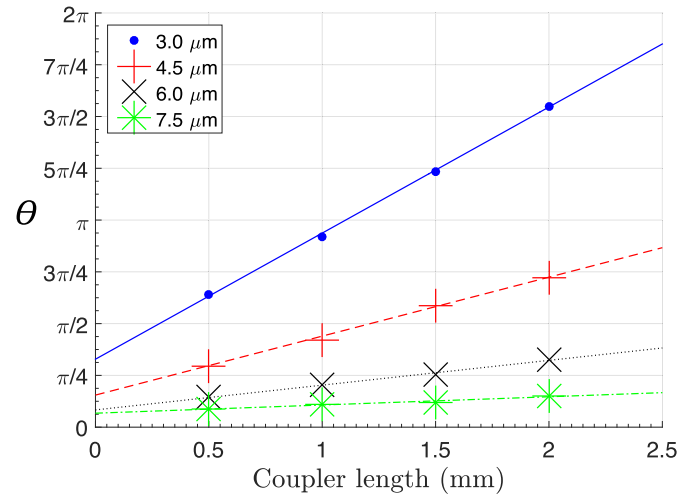
Fig. 7. Coupling phase θ as a function of the coupler length l_c for different waveguide separations d.

(3), correspond to $(\cos^2\theta|\sin^2\theta)$ and match the probability of detecting one photon at outputs 4 and 3. We must stress that at Table I there are two BIOEs that work approximately as a $X_{\pi/4}$ coupler and three as a $X_{\pi/2}$ coupler, which are the most interesting couplers for this work. These couplers, in (d,l_c) notation, are $(3.0, 1.5)$ and $(6.0, 1.5)$ for $X_{\pi/4}$, and $(4.5, 1.0)$, $(4.5, 1.5)$, and $(3.0, 2.0)$ for $X_{\pi/2}$. Although these couplers are suitable for our testing purposes, quasi-exact couplers $X_{\pi/4}$ and $X_{\pi/2}$ can be obtained by fitting a theoretical model to the experimental data shown in Table I. Indeed, the coupling phase (3) can be expressed as

$$\theta = \kappa l_c + \kappa \Delta l_c = \arccos \sqrt{P_4/(P_3+P_4)}, \qquad (16)$$

where Δl_c is an effective length corresponding to the interaction before and after the region defined by l_c, that is, in the sections described by the Minford curve (15). We must stress that the experimental values of θ (right-hand side of (16)) belong to the first quadrant, therefore they have to be properly unwrapped. In Fig. 7 we represent these values with respect to the coupler length l_c for the different values of the waveguide separations d. The
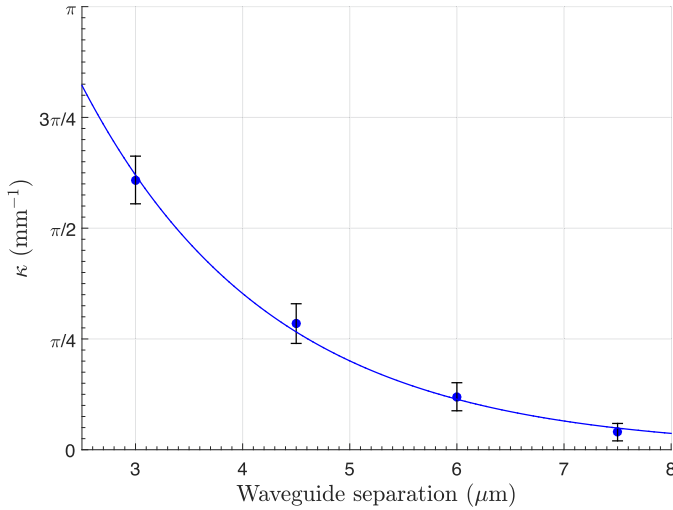
Fig. 8.   Coupling coefficient κ as a function of the waveguide separation d.
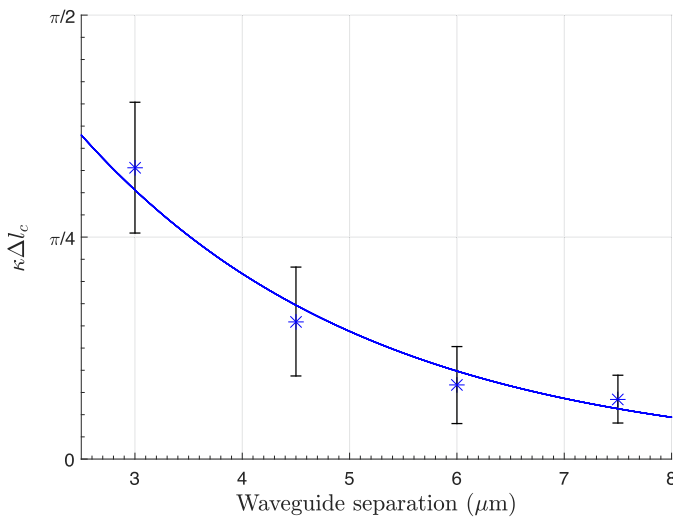

Fig. 9.   Term $\kappa \Delta l_c$ as a function of the waveguide separation d.

best linear fit to the data is also shown. It is clearly seen how the coupling phase grows linearly with the coupler length. Besides, in the different curves we see that, the closer the waveguides are, the faster the coupling phase grows, as the coupling, given by the coefficient κ, is stronger. With respect to this coefficient, the coupled mode theory [24] shows that it is directly related to the overlap of the evanescent exponential fields of the optical modes outside the waveguide channels. Thus, the dependence between κ and the waveguide separation d is also expected to be exponential, that is,

$$\kappa = a \cdot \exp\left(-b \cdot d\right), \tag{17}$$

where a and b are empiric fitting parameters. In Figs. 8 and 9 we represent the coupling coefficients κ and the term $\kappa \Delta l_c$, taken from the best linear fits shown in Fig. 7, with respect to the waveguide separation d. The confidence intervals are also shown for a 95% confidence level. The best fit of (17) to these

data gives rise to the following empiric function for (16):

$$\theta = 3.372\pi \exp\left(-0.564\,d\right) l_c + 0.926\pi \exp\left(-0.372\,d\right), \tag{18}$$

where the fitting parameters has been obtained by minimizing the weighted root mean square error. This equation provides remarkable fabrication curves that enable the manufacture of any kind of coupler by K$^+$/Na$^+$ ion-exchange with waveguides whose mask width is s=3 μm and transitions defined by the Minford curve given by (15). With these curves, it is possible to fabricate different couplers X_θ by varying the separation and coupling length. However, as mentioned above, among the different BIOEs used for calibration, there is a almost perfect $X_{\pi/4}$ coupler, that is, an element that can be used to test the projections of states belonging to the bases X and Y.

The scalability of the proposed IQOC is primarily limited by the length of the S-shaped waveguides ($l_m \simeq 1.5$ mm), which limits the number of BIOEs that can be concatenated in a single chip. For example, a length of 10 mm is needed to implement the IQOP of Fig. 1, even choosing the shortest distances between the waveguides of the couplers. We could improve this through a redesign that removes unnecessary curves. Furthermore, the length l_m itself can be reduced by increasing the effective index, so that the waveguide admits greater curvatures. However, this also increases the length of the couplers for a given lithographic resolution, so a balance must be found. Although more studies are needed, a density of 5-10 couplers/cm seems possible, allowing for low and medium complexity IQOCs.

C. Semiclassical Test of the Integrated Projector

The projection test consists of introducing laser light with different relative phases ϵ into the two input channel waveguides of the directional coupler and observing the output as a function of these relative phases. This kind of illumination corresponds to a two-mode coherent state, that is,

$$|L\rangle = |\alpha_j \alpha_{j'}\rangle = |a_j e^{i\epsilon_j}\, a_{j'} e^{i\epsilon_{j'}}\rangle, \tag{19}$$

where j=3 and j'=4, because we turned around the BIOE and outputs 3 and 4 were used as inputs, and inputs 1 and 2 as outputs (see Fig. 4). This was done to prevent losses in the reference waveguide from distorting the results. Even so, some losses in output 1 due to the Y-junction were still observed. Thus, when light was coming entirely from output 1, its intensity was lower than when it was coming exclusively from output 2.

Different quantum states can be obtained by introducing different relative phases ϵ=ϵ_4-ϵ_3. In our experiment, this was done by inserting a diffraction grating (G) between the auxiliary lens L3 and the first beam splitter (BS), as it is shown in Fig. 5. This grating was also fabricated by ion-exchange, following the method described in reference [42]. Its period is $p = 60$ μm and it distributes light mostly between diffraction orders ± 1, allowing us to obtain two light beams (coherent states) with the same power ($|a_3|^2$=$|a_4|^2$=$|a_o|^2$). The grating mount allows micrometric motions along the Y and Z-axes. Both diffraction orders remain focused on the input face of the BIOE regardless the grating position. By moving axially the grating, we can adjust the distance between the focused beams and couple accurately
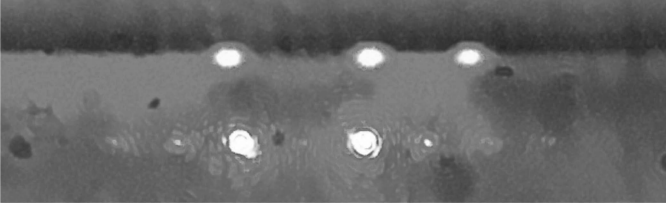
Fig. 10. Three channel waveguides (3, 4, and 5) of the BIOE (top) and the two focused diffracted beams (bottom), as observed through the eyepiece. Note that optical saturation of the camera produces a slightly distorted image.

each beam to its respective waveguide (3 and 4). It can be easily checked through the eyepiece, while the BIOE is backlit with a LED to highlight the waveguides (see Fig. 10). On the other hand, by moving transversally the grating (Y-axis), a phase shift $\pm 2\pi y/p$ is added in the respective order ± 1. Particularly, a displacement of half a period (30 μm) corresponds to a relative phase shift $\epsilon = 2\pi$. Therefore, the two-mode coherent states produced by the grating are given, to good approximation, by $|L\rangle = |a_o e^{-i\epsilon/2} a_o e^{i\epsilon/2}\rangle$. Now, let us consider a very weak coherent state, that is, $a_o \ll 1$, in such a way that we obtain the single photon state

$$|L\rangle \approx |0_3 0_4\rangle + a_o e^{-i\epsilon/2}|1_3 0_4\rangle + a_o e^{i\epsilon/2}|0_3 1_4\rangle. \quad (20)$$

Then, by taking into account the transformations of the operators corresponding to a X_θ coupler, the normalized detection probability of a photon coming from outputs 1 or 2 of the coupler is given by

$$\mathcal{P}_{1,2} = \frac{1}{2}(1 \pm \sin 2\theta \sin \epsilon), \quad (21)$$

which, except constants, corresponds to the classical light power. In short, a semiclassical analysis also provides a characterization of the IQOP for single photon states. So, a semiclassical test of the IQOP for analysing its capability for implementing projective measurements can be made.

The basic unit selected for testing is the one labelled by $(d, l_c) = (6.0, 1.5)$ in Table I, that is, a $X_{\pi/4}$ coupler. Once the two focused diffracted beams were coupled to its inputs 3 and 4, the diffraction grating was moved step by step along the Y-axis and, at the same time, light power was measured at both outputs 1 and 2. Moreover, due to losses in the Y-junction, the measured power at output 1 was corrected. This was done by taking into account that these losses are given by $(1-P_1 \text{m}/P_2 \text{m})$, being P_{im} the maximum measured power at outputs 1 and 2. Recall that the sample was turned around. The results of this optical characterization are represented in Fig. 11. They are compared to the theoretical curves given by (21). A sinusoidal behaviour of the light power, as a function of the grating displacement, is observed at both outputs. Maximum and minimum experimental values do not reach 1 and 0 because the coupler is not exactly a $X_{\pi/4}$ and there is some backlight that affects the measurements. We also observe that a full cycle is completed for a displacement of 30 μm.

The most remarkable cases are those ones corresponding to phase shifts $\epsilon = \pi/2$ and $3\pi/2$, because they simulate projective measurements of the quantum states belonging to bases X and Y,
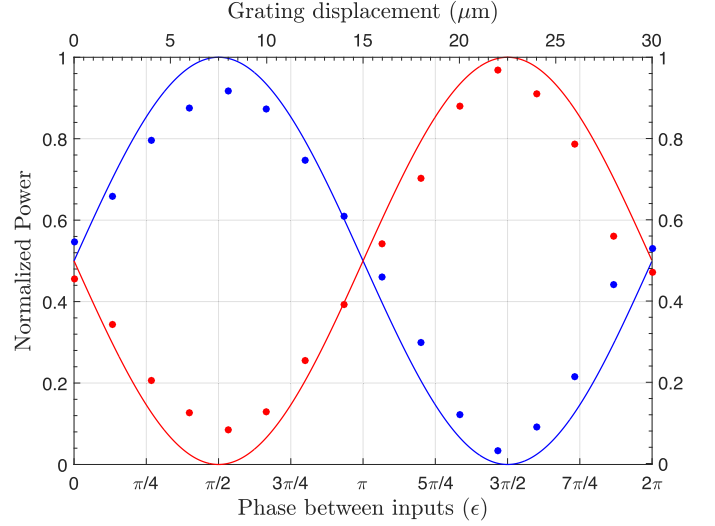

Fig. 11. Normalized light power measured at both outputs (blue and red dots) as a function of both the grating displacement (upper X-axis) and the phase between beams (lower X-axis). The theoretical curves (21) for a $X_{\pi/4}$ coupler are also represented (blue line for output 1 and red line for output 2).
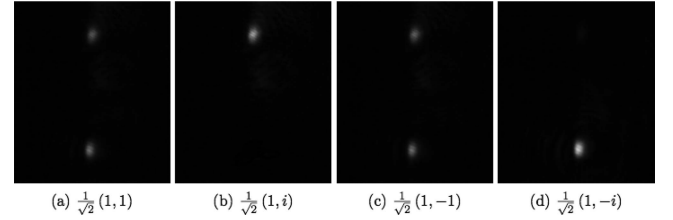

Fig. 12. Output power after introducing two light beams with phase shift ϵ in both inputs. (a) $\epsilon = 0$, (b) $\epsilon = \pi/2$, (c) $\epsilon = \pi$, (d) $\epsilon = 3\pi/2$. The input states simulated with these light beams are indicated.

which are commonly used in the BB84 protocol. Indeed, when the grating introduces phases $\epsilon = \pi/2$ and $3\pi/2$, basis Y is implemented and the output states are $i|1_1\rangle$ and $|1_2\rangle$, respectively. That is, the states of basis Y have been projected on the outputs 1 and 2. Fig. 12(b) and (d) show the experimental results of these projections. If input states were $|1_D\rangle$ and $|1_A\rangle$, the use of an additional phase shifter $Z_{\pi/2}$ would be required, as it was analysed in Section II. However, note that the above results, with the relative phases $\epsilon = \pi/2$ and $3\pi/2$ introduced by the grating, can be reinterpreted as if the input state were $(1/\sqrt{2})(|1_3\rangle \pm |1_4\rangle)$, but with an additional phase $\pi/2$ introduced by the grating acting as a gate $Z_{\pi/2}$. Therefore, we can implement the phase shifter $Z_{\pi/2}$ in this way. On the other hand, for phase shifts 0 and π, light comes out with almost the same intensity in both outputs (see Fig. 12(a) and (c)). This means that states $|1_D\rangle$ and $|1_A\rangle$ are eigenstates of the IQOP. In short, the directional coupler works as an IQOP for two-dimensional quantum states. In particular, for the states belonging to basis Y, that is, $|1_L\rangle$ and $|1_R\rangle$. For the states $|1_D\rangle$ and $|1_A\rangle$ of basis X a further relative phase $\pi/2$ must be introduced. This can be achieved by a $Z_{\pi/2}$ phase shifter, which can be easily implemented by changing, for instance, the length of the channel waveguides.

V. CONCLUSION

Ion-exchanged glass as a platform for quantum photonics has been proposed. We have demonstrated in such a platform passive quantum projections for the states of bases X (diagonal) and Y (circular) by using directional couplers which are constituted by single-mode channel waveguides fabricated by a K^+/Na^+ ion-exchange followed by a burial process. We have characterized these couplers and obtained empiric curves between both fabrication and optical parameters of such elements. In particular, we have modelled their coupling coefficient as an exponential function with respect to the separation of the channel waveguides. These results enable the fabrication of specific couplers, like $X_{\pi/4}$ and $X_{\pi/2}$, for producing integrated optical projectors for quantum optical processing devices and, in particular, for quantum cryptography, where a random choice of measurement basis is required. Likewise, a semiclassical optical test of a $X_{\pi/4}$ coupler has been made by using a diffraction grating to implement relative phases in single photon quantum states and thus to test the fabricated projectors. The projections have been obtained with an efficiency close to 1. Finally, these results can be used to produce quantum projectors of higher dimension ($d > 2$) or even to generate different quantum states, which is also an important task in quantum cryptography or in other devices for quantum information.

REFERENCES

[1] A. Politi, J. C. F. Matthews, M. G. Thompson, and J. L. O'Brien, "Integrated quantum photonics," *IEEE J. Sel. Topics Quantum Electron.*, vol. 15, no. 6, pp. 1673–1684, Nov./Dec. 2009.

[2] S. Bogdanov, M. Y. Shalaginov, A. Boltasseva, and V. M. Shalaev, "Material platforms for integrated quantum photonics," *Opt. Mater. Exp.*, vol. 7, no. 1, pp. 111–132, Jan. 2017.

[3] J. Wang, A. Sciarrinom, F. Laing, and M. Thompson, "Integrated photonic quantum technologies," *Nature Photon.*, vol. 14, no. 5, pp. 273–284, 2020.

[4] J. Liñares, M. Nistal, D. Barral, V. Moreno, C. Montero, and X. Prieto, "Quantum integrated optics: Theory and applications," *Optica Pura y Aplicada*, vol. 44, pp. 241–253, 2011.

[5] G. C. Righini and J. Liñares, "Active and quantum integrated photonic elements by ion exchange in glass," *Appl. Sci.*, vol. 11, no. 11, Jun. 2021, Art. no. 5222.

[6] T. Hurvitz, S. Ruschin, D. Brooks, G. Hurvitz, and E. Arad, "Variable optical attenuator based on ion-exchange technology in glass," *J. Lightw. Technol.*, vol. 23, no. 5, pp. 1918–1922, 2005.

[7] M. Fox, *Quantum Optics*. London, U.K.: Oxford Univ. Press, 2006.

[8] G. Agarwal, *Quantum Optics*. Cambridge, U.K.: Cambridge Univ. Press, 2013.

[9] M. Nielsen and I. Chuang, *Quantum Computation and Quantum Information: 10th Anniversary Edition*. Cambridge, U.K.: Cambridge Univ. Press, 2010.

[10] T. Hayashi and T. Nakanishi, "Multi-core optical fibers for the next-generation communications," *SEI Tech. Rev.*, vol. 86, pp. 23–28, 2018.

[11] G. Cañas et al., "High-dimensional decoy-state quantum key distribution over multicore telecommunication fibers," *Phys. Rev. A*, vol. 96, Aug. 2017, Art. no. 022317.

[12] D. Balado, J. Liñares, X. Prieto-Blanco, and D. Barral, "Phase and polarization autocompensating N-dimensional quantum cryptography in multicore optical fibers," *JOSA B*, vol. 36, pp. 2793–2803, 2019.

[13] N. Bai et al., "Mode-division multiplexed transmission with inline few-mode fiber amplifier," *Opt. Exp.*, vol. 20, no. 3, pp. 2668–2680, Jan. 2012.

[14] D. Balado-Souto, J. Liñares, and X. Prieto-Blanco, "Phase auto-compensating high-dimensional quantum cryptography in elliptical-core few-mode fibres," *J. Modern Opt.*, vol. 66, pp. 947–957, 2019.

[15] S. Leon-Saval, A. Argyros, and J. Bland-Hawthorn, "Photonic lanterns," *Nanophotonics*, vol. 2, pp. 429–440, 2013.

[16] C. Doerr, "Silicon photonic integration in telecommunications," *Front. Phys.*, vol. 3, pp. 7–22, 2015.

[17] S. Longui and G. D. Valle, "Anyons in one-dimensional lattices: A photonic realization," *Opt. Lett.*, vol. 37, pp. 2160–2162, 2012.

[18] J. Liñares, X. Prieto-Blanco, G. M. Carral, and M. C. Nistal, "Quantum photonic simulation of spin-magnetic field coupling and atom-optical field interaction," *Appl. Sci.*, vol. 10, 2020, Art. no. 8850.

[19] L. Sansoni et al., "Two-particle bosonic-fermionic quantum walk via integrated photonics," *Phys. Rev. Lett.*, vol. 108, 2012, Art. no. 010502.

[20] J. Matthews and M. Thompson, "An entangled walk of photons," *Nature*, vol. 484, pp. 47–48, 2012.

[21] E. Polino et al., "Experimental multiphase estimation on a chip," *Optica*, vol. 6, pp. 288–295, 2019.

[22] E. Polino, M. Valeri, N. Spagnolo, and F. Sciarrino, "Photonic quantum metrology," *AVS Quantum Sci.*, vol. 2, 2020, Art. no. 024703.

[23] M. Barbieri, "Optical quantum metrology," *PRX Quantum*, vol. 3, 2022, Art. no. 010202.

[24] D. Lee, *Electromagnetic Principles of Integrated Optics*. New York, NY, USA: Wiley, 1986.

[25] S. I. Najafi, *Introduction to Glass Integrated Optics*. Boston, MA, USA: Artech House, 1986.

[26] J. Liñares et al., "Glass processing by ion exchange to fabricate integrated optical planar components: Applications," in *Proc. SPIE Integr. Opt. Devices IV*, 2000, pp. 227–238.

[27] G. C. Righini, G. N. Conti, and M. A. Forastiere, "Integrated optical directional couplers: How much effective are design and modeling for device production?," in *Proc. SPIE Integr. Opt. Devices: Potential Commercialization*, 1997, pp. 212–219.

[28] J. Spring et al., "Boson sampling on photonic chip," *Science*, vol. 339, pp. 798–801, 2013.

[29] N. Gisin, G. Ribordy, W. Tittel, and H. Zbinden, "Quantum cryptography," *Phys. Rev. A*, vol. 74, pp. 145–194, 2002.

[30] A. Chefles, "Quantum state discrimination," *Contemporary Phys.*, vol. 41, no. 6, pp. 401–424, 2000.

[31] G. L. Yip and J. Finak, "Directional-coupler power divider by two-step K^+-ion exchange," *Opt. Lett.*, vol. 9, pp. 423–425, 1984.

[32] A. N. Miliou, R. Srivastava, and R. V. Ramaswamy, "Modeling of the index change in $K^+–Na^+$ ion-exchanged glass," *Appl. Opt.*, vol. 30, no. 6, pp. 674–681, Feb. 1991.

[33] J. Liñares, C. Montero, X. Prieto, and R. de La Fuente, "Simultaneous characterization of surface and buried waveguides produced by ion exchange in glass," *J. Modern Opt.*, vol. 41, pp. 5–9, 1994.

[34] A. Tervonen, B. R. West, and S. Honkanen, "Ion-exchanged glass waveguide technology: A review," *Opt. Eng.*, vol. 50, 2011, Art. no. 071107.

[35] J. Liñares, V. Moreno, and M. Nistal, "Designing of monomode step-index channel guides with quasi-exact modal solutions by the effective index method," *J. Modern Opt.*, vol. 47, no. 4 pp. 599–604, 2000.

[36] J. Liñares, V. Moreno, M. Nistal, and J. Salgueiro, "Modeling of ion-exchanged monomode channel guides with quasi-exact solutions by the effective index method," *J. Modern Opt.*, vol. 48, no. 5, pp. 789–795, 2001.

[37] C. Montero-Orille, X. Prieto-Blanco, H. González-Núñez, and J. Liñares, "A polygonal model to design and fabricate ion-exchanged diffraction gratings," *Appl. Sci.*, vol. 11, no. 4, Feb. 2021, Art. no. 1500.

[38] R. G. Walker and C. D. W. Wilkinson, "Integrated optical waveguiding structures made by silver ion-exchange in glass. 2: Directional coupler and bends," *Appl. Opt.*, vol. 22, no. 12, pp. 1929–1936, Jun. 1983.

[39] W. J. Minford, S. K. Korotky, and R. C. Alferness, "Low-loss Ti:LiNbO3 waveguide bends at 1.3 μm," *IEEE J. Quantum Electron.*, vol. QE-18, pp. 1802–1905, 1994.

[40] X. Prieto-Blanco and J. Liñares, "Two-mode waveguide characterization by intensity meaurements from exit face images," *IEEE Photon. J.*, vol. 4, no. 1, pp. 65–79, Feb. 2012.

[41] S. T. Popescu, P. S. Gheorghe, and A. Petris, "Measuring very low optical powers with a common camera," *Appl. Opt.*, vol. 53, no. 24, pp. 5460–5464, Aug. 2014.

[42] C. Montero-Orille et al., "Optimising zero-order suppression in ion-exchanged phase gratings," in *Proc. EPJ Web Conf.*, 2020, Art. no. 03006.